Supporting Information

Self-Assembly-Driven Nanodot Confinement of and Interfacial Engineering of Cobalt Metaphosphates for Electrocatalytic Oxygen Evolution

Junzheng Wei,[a] Qifu Zhang,[a] Yongda Guo,[a] Minling Zheng,[a] Yating Hu,[a*] Xin Li,[b*] and Shaoming Huang[c*]

Experimental Section

***Chemicals*:** Cobalt chloride hexahydrate ($CoCl_2 \cdot 6H_2O$, Macklin, 99%), Sodium hydroxide (*NaOH*, AR), n-Hexylphosphonic acid (*HPA*, Macklin, 98 %), Lauric acid ($C_{12}H_{24}O_2$, Macklin, 98 %), n-Hexane (C_6H_{14}, Macklin, ≥98 %, GC), N, N-Dimethylfornanide (*DMF*, Macklin, 99.5 %), Nafion® perfluorinated resin-aqueous dispersion (Aladdin, 5 wt.% in water), Carbon black (Macklin, xc-72R, 10-20 nm) and ethanol (CH_3CH_2OH, Macklin, 95 %).

***Synthesis of Co_3O_4 nano-size octahedra*:** Co_3O_4 nano-size octahedra was synthesized following a hydrothermal method reported by Huang et al[1].

***Synthesis of Co-HPA*:** 1 mmol of Co_3O_4 nano-size octahedra was dispersed and ultrasonicated in 6 ml of n-hexane for 30 min. Subsequently, 8 mmol of HPA and 30 g of lauric acid were added. The mixture was heated to 60 ℃ under vigorous stirring, with N_2 gas purged it for 1 hour to remove n-hexane and air. Then, the Co_3O_4 nano-size octahedra and HPA in lauric acid solution were heated up to 280 ℃ under N_2 atmosphere and refluxed at this temperature for 6 h. After heating was completed, the mixture was cooled to 60 ℃, followed by the addition of 50 ml DMF and stirring. Co-HPA precipitates was then collected by centrifugation. The precipitates were washed by DMF for 3 times and ethanol for 1 time to remove the residues of HPA and lauric acid. After drying in oven at 60 ℃ and grinding treatment, a grey powder was collected.

***Synthesis of Cobalt metaphosphate*:** The as-synthesized Co-HPA powder was placed in an alumina crucible and then placed in a tube furnace for heat treatment under N_2 atmosphere until the furnace was cooled down to below 60 ℃.

***Material Characterizations*:** The samples were analyzed using X-ray diffraction (XRD), transmission electron microscopy (TEM), Scanning electron spectroscopy (SEM), Energy-dispersive X-ray analysis (EDX), Thermal gravimetric analysis (TGA), N_2 adsorption isotherm at 77 K, Raman spectroscopy and Fourier transform infrared (FTIR) spectroscopy. XRD patterns were obtained using a SmartLabTM 9 kW X-ray diffractometer (Cu Kα radiation, λ=1.541 Å). TGA was done using SDT Q600 and N_2 adsorption isotherm was tested by Micromeritics ASAP 2460 instrument. Scanning

electron microscopy (SEM) images were captured using a FEI Apreo C microscope, allowing for high-resolution imaging and analysis of the samples. Transmission electron microscopy (TEM) measurements were performed on a FEI Talos F200S 200 kV transmission electron microscope, coupled with a Super-XEDS for dispersive X-ray spectroscopy (EDS) and elemental mapping.

***Electrochemical measurements and calculations*:** The oxygen evolution reaction (OER) catalytic activities of samples were studied in a standard three-electrode system in O_2 saturated 1 M KOH electrolyte (pH = 12.93) using Vertex. C. EIS. Pt plate and saturated calomel electrode (SCE) were used as the counter and reference electrodes, respectively. The linear sweep voltammetry (LSV) curves were recorded with sweeping rate of 50 mV s^{-1}. All potentials are referred to RHE. $E_{RHE} = E_{SCE\ (3\ M\ KCl)} + 0.234\ V + 0.059\ V \times pH$.

Computational Methods: Density functional theory computations were performed using the Vienna Ab initio Simulation Package version 5.4.4 with the projector augmented wave method to describe ion-electron interactions. The electronic wave functions were expanded utilizing a plane-wave basis set with a kinetic energy cutoff of 500 eV. Geometric optimization was first conducted on the bulk unit cell of $Co_2P_4O_{12}$ to obtain the ground state structure as depicted in Figure S10a. The (022) facet was identified as the dominant exposed surface based on experimental X-ray diffraction patterns and was consequently selected for surface modeling. A vacuum layer of 15 Å was applied along the z-direction to eliminate spurious interactions between periodic images. The optimized bulk structure was cleaved along this plane to generate the surface slab models shown in Figure S10b. To mimic the bulk environment constraints during surface relaxation, atoms in the bottom three layers were fixed at their bulk positions while the upper layers were allowed to relax fully. Brillouin zone integration employed the Monkhorst-Pack scheme with a k-point grid density of approximately 0.03 $Å^{-1}$ for bulk calculations and a 3×3×1 mesh for the surface slab calculations.

The electrocatalytic oxygen evolution reaction activity was evaluated assuming the adsorbate evolution mechanism (AEM) in alkaline media. This pathway involves four concerted proton-electron transfer steps associated with the sequential formation of

*OH, *O, and *OOH intermediates on the active site. The elementary reaction steps proceed according to the following equations

$* + OH^- \rightarrow *OH + e^-$

$*OH + OH^- \rightarrow *O + H_2O + e^-$

$*O + OH^- \rightarrow *OOH + e^-$

$*OOH + OH^- \rightarrow * + O_2 + H_2O + e^-$

The asterisk denotes the active site on the catalyst surface. The Gibbs free energy change for each elementary step was determined using the computational hydrogen electrode model. This value is defined by the equation $\Delta G = \Delta E + \Delta E_{ZPE} - T\Delta S - eU$. Here ΔE represents the reaction energy difference obtained from DFT simulations and ΔE_{ZPE} denotes the change in zero-point energy. The entropy contribution is given by ΔS at standard temperature and U refers to the applied electrode potential. The theoretical overpotential was subsequently derived from the potential-determining step exhibiting the largest free energy change. This value is calculated by subtracting the equilibrium potential of 1.23 V from the maximum Gibbs free energy change divided by the elementary charge.

Table

Table S1. Nomenclature and heat-treatment conditions for various samples under N_2 atmospheres.

Sample Name	Temperature (℃)	Holding time (h)
ComP/$C_{500\text{-}3}$	500	3
ComP/$C_{500\text{-}6}$	500	6
ComP/$C_{550\text{-}3}$	550	3
ComP/$C_{550\text{-}8}$	550	8
ComP/$C_{600\text{-}3}$	600	3
ComP/$C_{700\text{-}3}$	700	3
ComP/$C_{800\text{-}3}$	800	3

Table S2. Co content and Mass activity (at 1.53V) of ComP/$C_{500\text{-}3}$, ComP/$C_{500\text{-}6}$, ComP/$C_{550\text{-}8}$, ComP/$C_{700\text{-}3}$.

Sample	Co(wt%)	Mass activity ($A \cdot g_{Co}^{-1}$@1.53V)
ComP/$C_{500\text{-}3}$	25.9	128.0
ComP/$C_{500\text{-}6}$	24.8	233.2
ComP/$C_{550\text{-}8}$	22.5	133.4
ComP/$C_{700\text{-}3}$	20.4	18.6

Table S3. ECSA and Specific activity (at 1.53V) of ComP/$C_{500\text{-}3}$, ComP/$C_{500\text{-}6}$, ComP/$C_{550\text{-}3}$, ComP/$C_{550\text{-}8}$, ComP/$C_{600\text{-}3}$, ComP/$C_{700\text{-}3}$.

Sample	ECSA (cm^2)	Specific activity（$mA \cdot cm_{ECSA}^{-2}$）
ComP/$C_{500\text{-}3}$	32.5	0.102
ComP/$C_{500\text{-}6}$	44.6	0.1295
ComP/$C_{550\text{-}3}$	35	0.073

ComP/$C_{550\text{-}8}$	26.6	0.113
ComP/$C_{600\text{-}3}$	36	0.0485
ComP/$C_{700\text{-}3}$	4.5	0.084

Table S4. Comparison of OER performance of recently reported cobalt phosphate-based catalysts in KOH solution.

Catalysts	**η10 (mV)**	**Tafel slope (mV dec^{-1})**	**References**
ComP/$C_{500\text{-}6}$	417	44.6	This work
$LiCoPO_4$/rGO	551	100	[2]
$Co_3(PO_4)_2$	561	109	[2]
Co_3O_4 NSs	540	234	[3]
R-Co_3O_4 NPs	430	92	[4]
$CoSe_2$ NSs	343	97.7	[5]
$CoSe_2$ NPs	466	111.1	[5]
CoO_x@CoN_y NRs	460	85.6	[6]
Co nanochains	390	120	[7]
CoO nanocubes	440	80.4	[7]
Co_3O_4	410	139	[8]
Co/NG	>500	178	[9]
Co/G	396	87	[9]
$Co(OH)_2$	380	53	[10]
$Na_2CoP_2O_7$	420	80	[11]
CoPi film	570	155	[12]
$Co_2P_4O_{12}$/CC	380	125	[13]
Co-phosphate	350	60.7	[14]
NCP@WPCA-0.5	351	94.44	[15]
ACTP5@Co,N-900	401	158	[16]
ACTP5@Co,N-800	374	98	[16]
$NaCo(PO_3)_3$	340	76	[17]

Figures

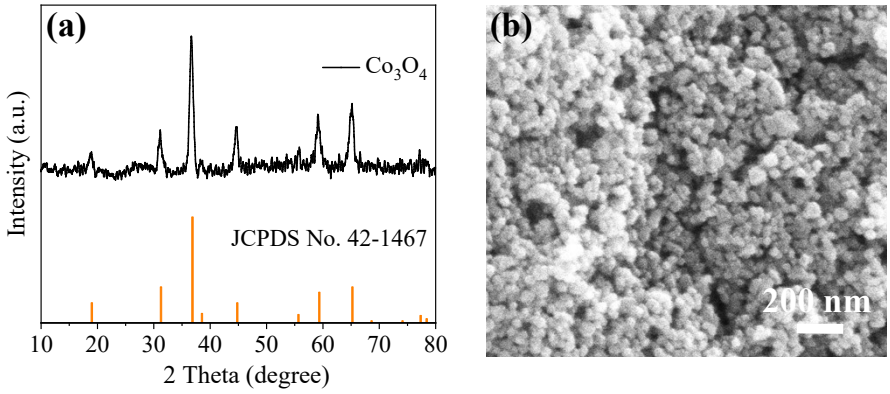

Figure S1. (a) XRD profile and (b) SEM image of Co_3O_4.

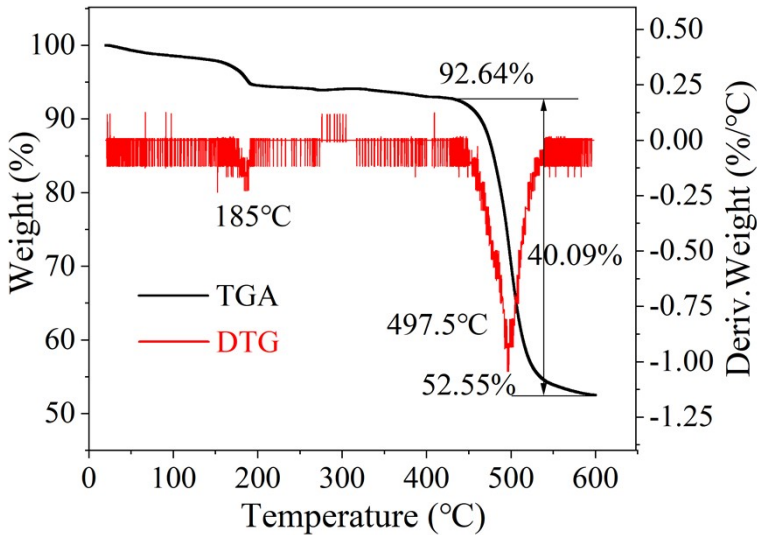

Figure S2. TGA and derivative thermogravimetry (DTG) curves for Co-HPA pyrolyzed in N_2 at the rate of 5 °C min^{-1}.

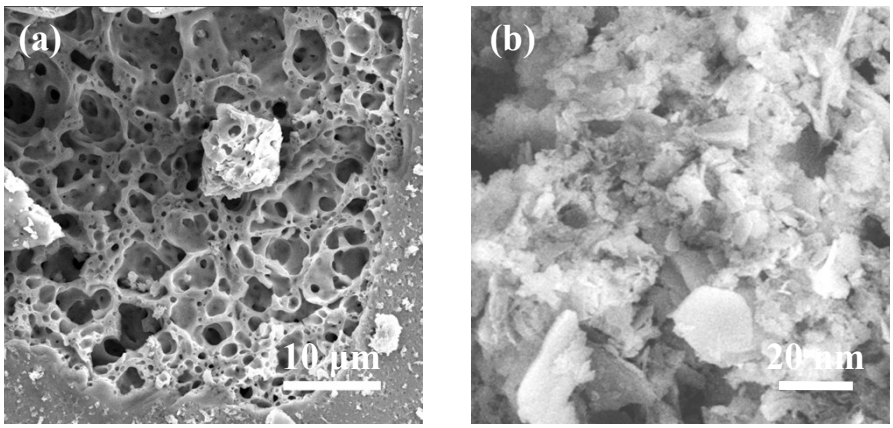

Figure S3. SEM images of ComP/$C_{550\text{-}8}$.

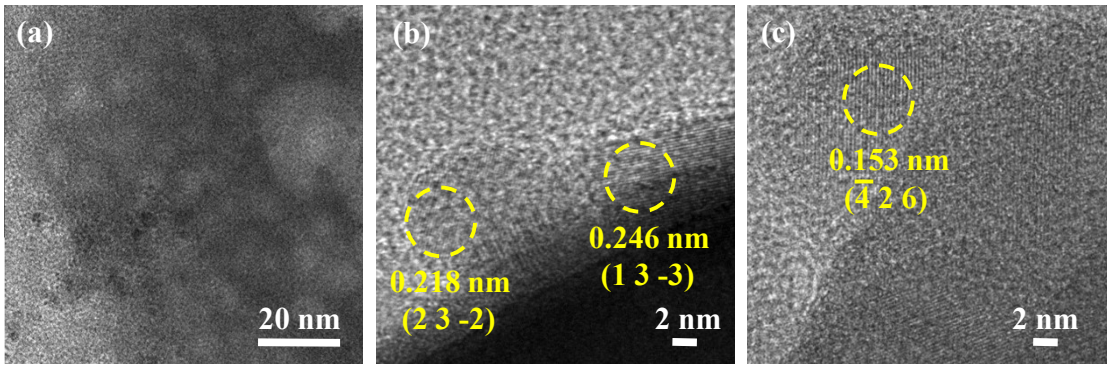

Figure S4. TEM images of (a) ComP/$C_{500\text{-}3}$, (b) ComP/$C_{600\text{-}3}$ and (c) ComP/$C_{700\text{-}3}$

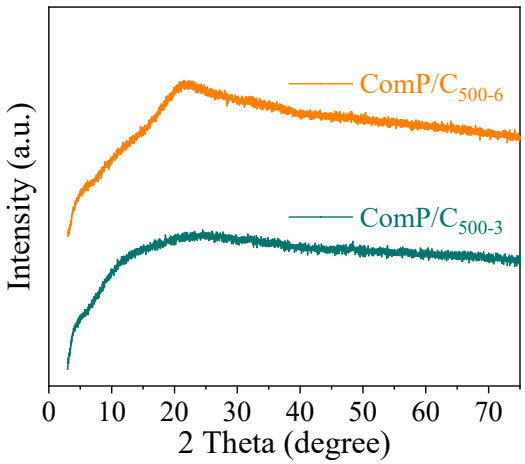

Figure S5. XRD profile of ComP/$C_{500\text{-}3}$ and ComP/$C_{500\text{-}6}$.

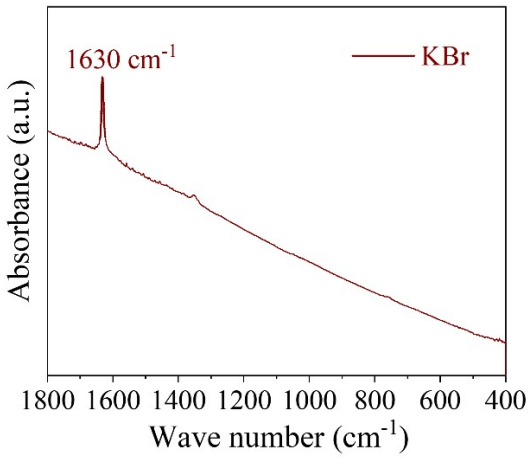

Figure S6. FTIR spectroscopy of KBr.

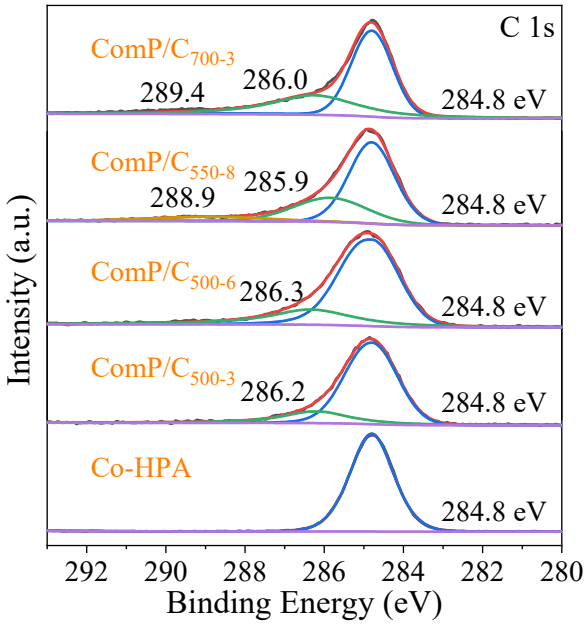

Figure S7. X-ray photoelectron spectra reveal the deconvoluted core level C 1s spectra of Co-HPA, ComP/$C_{500\text{-}3}$, ComP/$C_{500\text{-}6}$, ComP/$C_{550\text{-}8}$ and ComP/$C_{700\text{-}3}$.

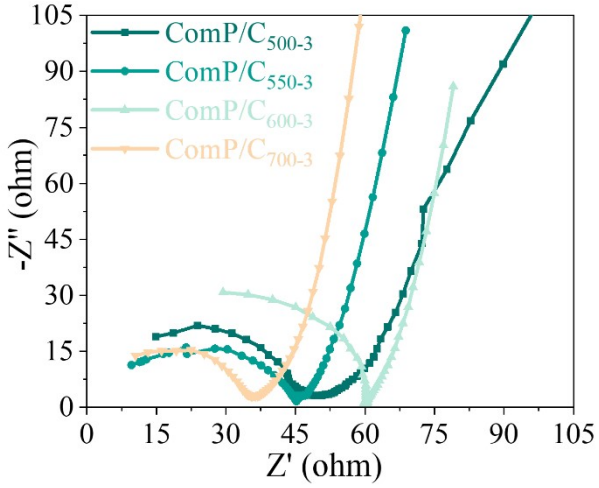

Figure S8. Nyquist plot of ComP/$C_{500\text{-}3}$, ComP/$C_{550\text{-}3}$, ComP/$C_{600\text{-}3}$, ComP/$C_{700\text{-}3}$.

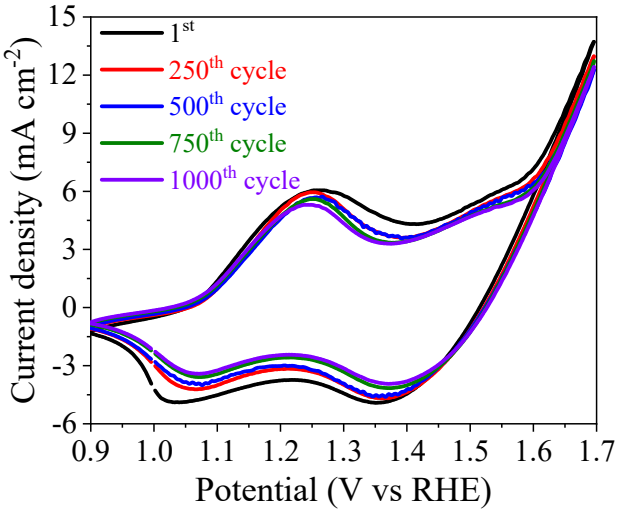

Figure S9. CV curves of ComP/$C_{500\text{-}6}$ at different cycle numbers.

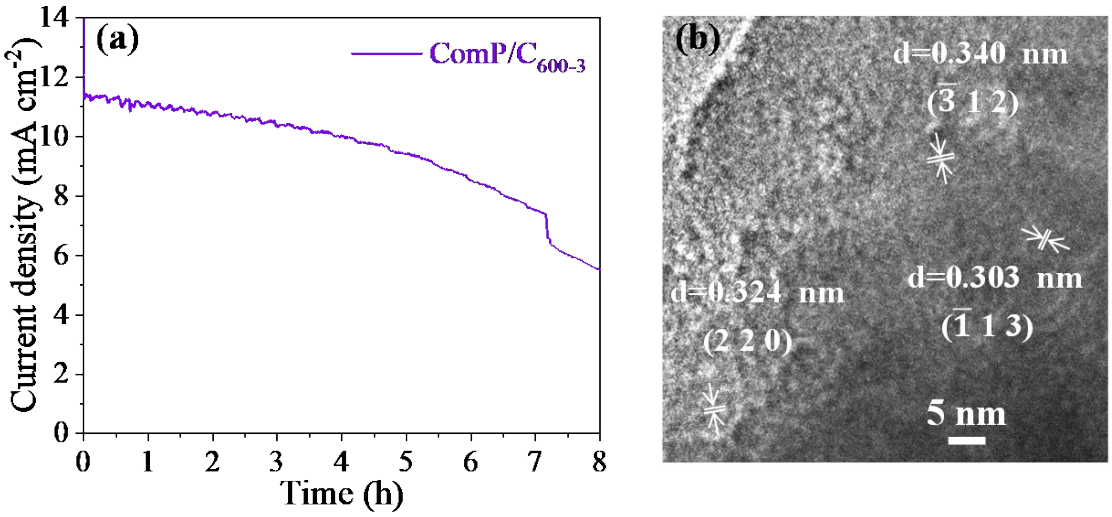

Figure S10. (a)Stability chronopotentiometry curve at 10 mA cm^{-2} of $ComP/C_{600\text{-}3}$. (b)Post-stability TEM images on $ComP/C_{600\text{-}3}$ after the chronopotentiometry test.

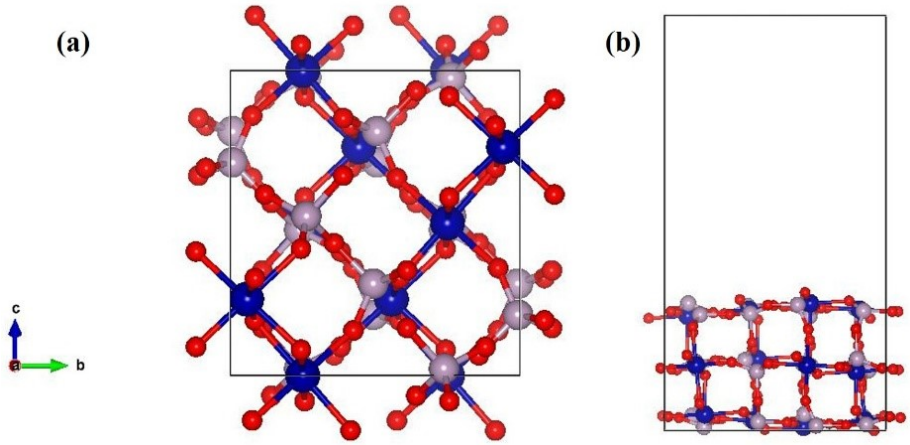

Figure S11. (a) Unit cells and (b) surface slab models of the $Co_2P_4O_{12}$ used for DFT calculations, with O, Co, and P atoms depicted as red, blue, and purple spheres, respectively.

References

[1] Huang Z., Zhao Y., Song Y., Li Y., Wu G., Tang H., and Zhao J., *RSC Advances*, **2016**. 6, 80059-80064

[2] Liu Y., Wang H., Lin D., Liu C., Hsu P.-C., Liu W., Chen W., and Cui Y., *Energy & Environmental Science*, **2015**. 8(6), 1719-1724.

[3] Xu L., Jiang Q., Xiao Z., Li X., Huo J., Wang S., and Dai L., *Angewandte Chemie International Edition*, **2016**. 55(17), 5277-5281.

[4] Zhou Y., Dong C.-K., Han L.-L., Yang J., and Du X.-W., *ACS CATALYSIS*, **2016**. 6(10), 6699-6703.

[5] Zhang Y., Zhang C., Guo Y., Liu D., Yu Y., and Zhang B., *Journal of Materials Chemistry A*, **2019**. 7(6), 2536-2540.

[6] Yoon K.R., Hwang C.-K., Kim S.-h., Jung J.-W., Chae J.E., Kim J., Lee K.A., Lim A., Cho S.-H., Singh J.P., Kim J.M., Shin K., Moon B.M., Park H.S., Kim H.-J., Chae K.H., Ham H.C., Kim I.-D., and Kim J.Y., *ACS Nano*, **2021**. 15(7), 11218-11230.

[7] Yuan X., Ge H., Wang X., Dong C., Dong W., Riaz M.S., Xu Z., Zhang J., and Huang F., *ACS Energy Letters*, **2017**. 2(5), 1208-1213.

[8] He D., Song X., Li W., Tang C., Liu J., Ke Z., Jiang C., and Xiao X., *Angewandte Chemie International Edition*, **2020**. 59(17), 6929-6935.

[9] Huang Q.e., Wang B., Ye S., Liu H., Chi H., Liu X., Fan H., Li M., Ding C., Li Z., and Li C., *ACS Catalysis*, **2022**. 12(1), 491-496.

[10] Liu J., Nai J., You T., An P., Zhang J., Ma G., Niu X., Liang C., Yang S., and Guo L., *Small*, **2018**. 14(17).

[11] Kim H., Park J., Park I., Jin K., Jerng S.E., Kim S.H., Nam K.T., and Kang K., *Nature Communications*, **2015**. 6(1), 8253.

[12] Zhang R., van Straaten G., di Palma V., Zafeiropoulos G., van de Sanden M.C.M., Kessels W.M.M., Tsampas M.N., and Creatore M., *ACS Catalysis*, **2021**. 11(5), 2774-2785.

[13] Chang X.W., Li S., Wang L., Dai L., Wu Y.P., Wu X.Q., Tian Y., Zhang S., and Li D.S., *Advanced Functional Materials*, **2024**. 34(21), 2313974

[14] Bhanja P., Kim Y., Paul B., Lin J., Alshehri S.M., Ahamad T., Kaneti Y.V., Bhaumik A., and Yamauchi Y., *ChemCatChem*, **2020**. 12(7), 2091-2096.

[15] Cui C., Lai X., Guo R., Ren E., Qin W., Liu L., Zhou M., and Xiao H., *Electrochimica Acta*, **2021**. 393, 139076.

[16] Zhang J., Zhang T., Ma J., Wang Z., Liu J., and Gong X., *Carbon*, **2021**. 172, 556-568.

[17] Gond R., Singh D.K., Eswaramoorthy M., and Barpanda P., *Angewandte Chemie International Edition*, **2019**. 58(25), 8330-8335.